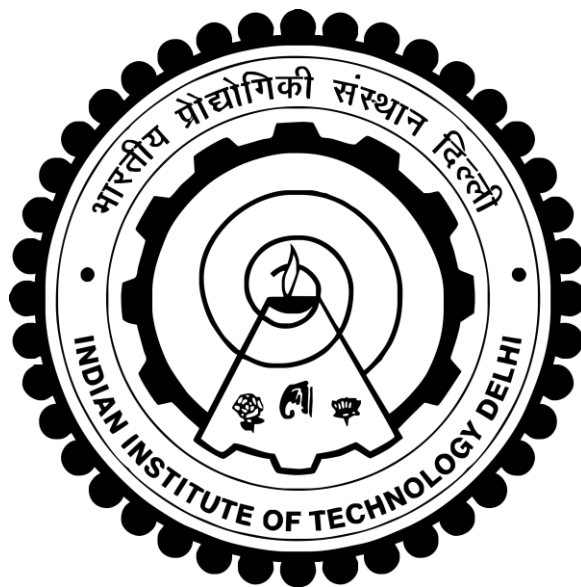


**ENGINEERING THE METAL OXIDE AND METAL SULFIDE
NANOSTRUCTURES FOR PHOTOELECTROCHEMICAL
AND PHOTOCATALYTIC WATER SPLITTING
APPLICATION**

JYOTI



**DEPARTMENT OF CHEMISTRY
INDIAN INSTITUTE OF TECHNOLOGY DELHI
OCTOBER 2024**

© Indian Institute of Technology Delhi (IITD), New Delhi, 2024

**Engineering the Metal Oxide and Metal Sulfide Nanostructures for
Photoelectrochemical and Photocatalytic Water Splitting Application**

by

Jyoti

Department of Chemistry

Submitted

In fulfilment of the requirements of the degree of Doctor of Philosophy

to the



Indian Institute of Technology Delhi

October 2024

Dedicated to my Parents

CERTIFICATE

This is to certify that the thesis entitled, “**Engineering the Metal Oxide and Metal Sulfide Nanostructures for Photoelectrochemical and Photocatalytic Water Splitting Application**” being submitted by **Miss Jyoti** to the **IITD-NYCU** joint Doctoral Program, **Indian Institute of Technology Delhi** for the award of the degree of **Doctor of Philosophy** in Chemistry, is a record of bonafide research work carried out by her. She has worked under our joint supervision and has fulfilled the requirements, which to our opinion has reached the requisite standard for the submission of the thesis.

Prof. Pravin P Ingole

Professor,

Department of Chemistry

Indian Institute of Technology, Delhi

Prof. Yung Jung Hsu

Professor,

Department of Material Science and Engineering

National Yang Ming Chiao Tung University, Taiwan

ACKNOWLEDGEMENTS

First and foremost, I would like to extend my heartfelt gratitude to my thesis supervisors, Prof. Pravin P. Ingole (IIT DELHI) and Prof. Yung Jung Hsu (NYCU, TAIWAN), for their unwavering guidance, patience, and support throughout this journey. Their confidence in my research has been a major source of motivation, ultimately enabling me to reach this goal. Their steadfast support, encouragement, and profound knowledge have been invaluable. Their continuous patience and timely advice have significantly broadened my perspectives and understanding. They have generously devoted substantial time to both technical and non-technical discussions, assisting me in preparing manuscripts for journals. Their contributions have been instrumental in shaping my research career.

I thank my SRC members profusely: Prof. Bijay P Tripathi, Prof. Ashok K Ganguli and Prof. Sameer Sapra, for their comments and suggestions to improve my work. I am thankful to IIT Delhi and NYCU Taiwan for the financial support. Also, I thank CRF, NRF, and the Chemistry department, IIT Delhi, and Material and Science department, NYCU for the research facilities. I would like to acknowledge all the heads of the chemistry department during this period.

Besides, I would like to extend my gratitude to all my friends, collaborators, and lab mates at IIT Delhi and NYCU Taiwan. I am especially thankful to Ms. Priya Jain, Ms. Cini M. Suresh, Dr. Dipika Sharma, and Mr. Aamir Bhat for their invaluable assistance in proofreading of my thesis. I am thankful to Mr. Ting-Hsuan Lai, Ms. Chun-Wen Tsao, and Mr. Hsuan-Hung Kuo for fostering a joyful environment, engaging in scientific discussions, and assisting me, making my stay in Taiwan memorable. I am also deeply indebted to Ms. Janet Alvarado for her love and care at NYCU Taiwan.

I must also highlight my wonderful friends, especially Ms. Rajat Joshi, Ms. Nidhi Gupta, Mr. Manu Garg, Ms. Sodabah Liaskhel and Ms. Swati Khurana, for being an integral part of my journey and enriching my experiences during my time at IIT Delhi and NYCU, Taiwan. Their companionship made life's adventures all the more beautiful.

Lastly, I want to express my profound gratitude to my entire family, especially my parents, brother, sister-in-law, and in-laws for their unconditional love, unwavering support, and constant encouragement. I am particularly thankful to my brother, Mr. Deepak, who has always stood by my side and encouraged me to achieve my life's goals.

Most importantly, I would like to express my deepest appreciation to my husband, Mr. Nitesh, for his love, care, and the courage he provides, enabling me to soar beyond limits. It is difficult for me to express my gratitude in words for him.

Jyoti

Abstract

Understanding the global energy landscape, which emphasizes on the need of transition to sustainable alternatives, as fossil fuels, which currently supply major part of global energy, decline. Solar energy, despite its intermittency, displays some potential. Photoelectrochemical (PEC) and photocatalytic (PC) water splitting are promising methods for converting solar energy into hydrogen. The heart of these processes is the photocatalyst, which should possess suitable band gaps, high absorption, effective charge separation, chemical stability and cost effective. In this connection, metal oxides and sulfides are promising due to their affordability and suitability. However, their activity remains low due to challenges like high electron-hole recombination and slow kinetics. This thesis is devoted towards the engineering of metal oxide and metal sulfide photocatalysts for enhanced PEC and PC activity.

Chapter 1, begins with discussion of the current energy landscape, stressing the need for renewable energy alternatives to fossil fuels. It underscores the significance of hydrogen as a clean energy source and explores various methods of hydrogen production. The chapter places particular emphasis on solar energy, highlighting its potential for generating hydrogen fuel through photoelectrochemical (PEC) and photocatalytic (PC) water splitting. Additionally, it delves into the mechanisms underlying this water splitting processes, providing a comprehensive discussion on the selection and properties of materials crucial for efficient PEC and PC water splitting.

In Chapter 2, we present the synthesis methods employed in the thesis, the preparation of electrodes and cell setups, and the various characterization techniques used to investigate the properties of semiconductor photocatalyst materials, whether in the form of powder or electrode. It also describes the various characterization techniques utilized throughout the

thesis. Additionally, we outline the methodology for conducting PEC and PC water splitting experiments.

In **Chapter 3**, we investigated the modulation of the bulk properties of g-C₃N₄ through the formation of Ni/NiO/g-C₃N₄ nanocomposites for photoelectrochemical (PEC) water splitting. We elucidated the critical role of active sites in enhancing PEC activity within these nanocomposites. Specifically, NiO facilitates the separation of photogenerated charge carriers by establishing a type-II heterojunction, while metallic Ni promotes the exfoliation of bulk g-C₃N₄ sheets into thinner layers. This exfoliation process reduces charge transfer resistance at the interface, thereby improving PEC activity. These findings highlight the significant contributions of Ni and NiO to the enhancement of the PEC properties of g-C₃N₄.

In **Chapter 4**, we focus on enhancing the surface properties of Hematite (Fe₂O₃) for photoelectrochemical (PEC) water splitting applications. Hematite is hampered by poor charge transfer dynamics and sluggish surface reaction kinetics, which limit its efficiency. To address this, we decorated the surface of Fe₂O₃ with a MnO_x co-catalyst. Optimal deposition of the co-catalyst, achieved with a deposition time of 100 seconds, significantly improves the electrochemically active sites and charge carrier density, thereby enhancing PEC activity. However, excessive deposition of the co-catalyst leads to increased back recombination, known as shunting, which diminishes PEC performance. This study provides a mechanistic understanding of the role of MnO_x as a co-catalyst in improving the PEC performance of semiconductor photoanodes.

In **Chapter 5**, we investigate ternary metal sulfide Au@Ag/AgCuS yolk@shell nanostructures for photocatalytic (PC) hydrogen generation, employing a successive ion exchange method for synthesis. The primary focus of this study is to examine the effect of void space on the PC

hydrogen generation rate. Precise adjustment of the void space allowed us to evaluate its impact on hydrogen production, revealing that larger void spaces exhibit superior photocatalytic performance, achieving a hydrogen generation rate of $1.65 \mu\text{mol h}^{-1}$ and an apparent quantum yield of 5.43% at 840 nm. Additionally, we underscore the importance of the yolk@shell nanostructure compared with hollow structures, finding shows that yolk@shell nanostructures show quite high hydrogen generation rate compared to hollow one, because in yolk@shell configuration enhances electron transfer between the Au core and the Ag/AgCuS shell, facilitated by upward band bending at the interface, as confirmed by ultraviolet photoelectron spectroscopy (UPS). This study underscores the significance of yolk@shell nanostructures and the influence of void space on PC hydrogen generation.

In **Chapter 6**, by tuning the Cu/In ratio, we elucidate the role of cation ratio in determining the PC hydrogen generation rate in Au-CuInS₂ (Au-CIS) yolk@shell nanostructures. An increased indium content relative to copper within the matrix elevates the work function, thereby enhancing hydrogen production rates. This improvement is attributed to efficient charge transfer between the Au core and the CuInS₂ yolk, facilitated by upward band bending at the interface. This study highlights the significant impact of cation ratio on PC hydrogen generation.

Overall, this thesis is devoted to tune the metal-oxide and metal sulfide semiconductors' properties using various strategies to boost their Photoelectrochemical (PEC) and photocatalytic (PC) hydrogen efficiency.

अमूर्त

वैश्विक ऊर्जा परिदृश्य को समझना, जो टिकाऊ विकल्पों में परिवर्तन की आवश्यकता पर जोर देता है, क्योंकि जीवाश्म ईंधन, जो वर्तमान में वैश्विक ऊर्जा का प्रमुख हिस्सा प्रदान करता है, में गिरावट आ रही है। सौर ऊर्जा, अपनी रुक-रुक कर होने के बावजूद, कुछ क्षमता प्रदर्शित करती है। फोटोइलेक्ट्रोकेमिकल (पीईसी) और फोटोकैटलिटिक (पीसी) जल विभाजन सौर ऊर्जा को हाइड्रोजन में परिवर्तित करने के आशाजनक तरीके हैं। इन प्रक्रियाओं का केंद्र फोटोकैटलिस्ट है, जिसमें उपयुक्त बैंड अंतराल, उच्च अवशोषण, प्रभावी चार्ज पृथक्करण, रासायनिक स्थिरता और लागत प्रभावी होना चाहिए। इस संबंध में, धातु ऑक्साइड और सल्फाइड अपनी सामर्थ्य और उपयुक्तता के कारण आशाजनक हैं। हालाँकि, उच्च इलेक्ट्रॉन-छिद्र पुनर्संयोजन और धीमी गतिकी जैसी चुनौतियों के कारण उनकी गतिविधि कम रहती है। यह थीसिस उन्नत पीईसी और पीसी गतिविधि के लिए धातु ऑक्साइड और धातु सल्फाइड फोटोकैटलिस्ट की इंजीनियरिंग के लिए समर्पित है।

अध्याय 1, वर्तमान ऊर्जा परिदृश्य की चर्चा से शुरू होता है, जिसमें जीवाश्म ईंधन के लिए नवीकरणीय ऊर्जा विकल्पों की आवश्यकता पर बल दिया गया है। यह एक स्वच्छ ऊर्जा स्रोत के रूप में हाइड्रोजन के महत्व को रेखांकित करता है और हाइड्रोजन उत्पादन के विभिन्न तरीकों की पड़ताल करता है। अध्याय सौर ऊर्जा पर विशेष जोर देता है, फोटोइलेक्ट्रोकेमिकल (पीईसी) और फोटोकैटलिटिक (पीसी) जल विभाजन के माध्यम से हाइड्रोजन ईंधन उत्पन्न करने की इसकी क्षमता पर प्रकाश डालता है। इसके अतिरिक्त, यह इस जल विभाजन प्रक्रियाओं के अंतर्निहित तंत्रों की गहराई से पड़ताल करता है, और कुशल पीईसी और पीसी जल विभाजन के लिए महत्वपूर्ण सामग्रियों के चयन और गुणों पर एक व्यापक चर्चा प्रदान करता है।

अध्याय 2 में, हम थीसिस में नियोजित संश्लेषण विधियों, इलेक्ट्रोड और सेल सेटअप की तैयारी, और अर्धचालक फोटोकैटलिस्ट सामग्री के गुणों की जांच करने के लिए उपयोग की जाने वाली विभिन्न लक्षण

वर्णन तकनीकों को प्रस्तुत करते हैं, चाहे वह पाउडर या इलेक्ट्रोड के रूप में हो। यह संपूर्ण थीसिस में प्रयुक्त विभिन्न लक्षण वर्णन तकनीकों का भी वर्णन करता है। इसके अतिरिक्त, हम पीईसी और पीसी जल विभाजन प्रयोगों के संचालन की पद्धति की रूपरेखा तैयार करते हैं।

अध्याय 3 में, हमने फोटोइलेक्ट्रोकेमिकल (पीईसी) जल विभाजन के लिए नी/नीओ/जी-सी₃एन₄ नैनोकम्पोजिट के निर्माण के माध्यम से जी-सी₃एन₄ के थोक गुणों के मॉड्यूलेशन की जांच की। हमने इन नैनोकम्पोजिट्स के भीतर पीईसी गतिविधि को बढ़ाने में सक्रिय साइटों की महत्वपूर्ण भूमिका को स्पष्ट किया। विशेष रूप से, NiO टाइप-II हेटेरोजंक्शन स्थापित करके फोटोजेनरेटेड चार्ज कैरियर्स को अलग करने की सुविधा प्रदान करता है, जबकि धात्विक Ni बल्क जी-सी₃एन₄ शीट्स को पतली परतों में एक्सफोलिएशन को बढ़ावा देता है। यह एक्सफोलिएशन प्रक्रिया इंटरफ़ेस पर चार्ज ट्रांसफर प्रतिरोध को कम करती है, जिससे पीईसी गतिविधि में सुधार होता है। ये निष्कर्ष जी-सी₃एन₄ के पीईसी गुणों को बढ़ाने में नी और नीओ के महत्वपूर्ण योगदान को उजागर करते हैं।

अध्याय 4 में, हम फोटोइलेक्ट्रोकेमिकल (पीईसी) जल विभाजन अनुप्रयोगों के लिए हेमेटाइट (Fe₂O₃) की सतह के गुणों को बढ़ाने पर ध्यान केंद्रित करते हैं। हेमेटाइट खराब चार्ज ट्रांसफर गतिशीलता और सुस्त सतह प्रतिक्रिया कैनेटीक्स से बाधित होता है, जो इसकी दक्षता को सीमित करता है। इसे संबोधित करने के लिए, हमने Fe₂O₃ की सतह को MnO_x सह-उत्प्रेरक से सजाया। सह-उत्प्रेरक का इष्टतम जमाव, 100 सेकंड के जमाव समय के साथ हासिल किया गया, इलेक्ट्रोकेमिकल रूप से सक्रिय साइटों और चार्ज वाहक घनत्व में काफी सुधार करता है, जिससे पीईसी गतिविधि में वृद्धि होती है। हालाँकि, सह-उत्प्रेरक के अत्यधिक जमाव से बैक पुनर्संयोजन में वृद्धि होती है, जिसे शंटिंग के रूप में जाना जाता है, जो पीईसी प्रदर्शन को कम कर देता है। यह अध्ययन सेमीकंडक्टर फोटोएनोड के पीईसी प्रदर्शन को बेहतर बनाने में सह-उत्प्रेरक के रूप में एमएनओएक्स की भूमिका की यंत्रवत समझ प्रदान करता है।

अध्याय 5 में, हम फोटोकैटलिटिक (पीसी) हाइड्रोजन उत्पादन के लिए टर्नरी मेटल सल्फाइड Au@Ag/AgCuS जर्दी@शेल नैनोस्ट्रक्चर की जांच करते हैं, जो संश्लेषण के लिए क्रमिक आयन विनिमय

विधि का उपयोग करते हैं। इस अध्ययन का प्राथमिक फोकस पीसी हाइड्रोजन उत्पादन दर पर शून्य स्थान के प्रभाव की जांच करना है। शून्य स्थान के सटीक समायोजन ने हमें हाइड्रोजन उत्पादन पर इसके प्रभाव का मूल्यांकन करने की अनुमति दी, जिससे पता चला कि बड़े शून्य स्थान बेहतर फोटोकैटलिटिक प्रदर्शन प्रदर्शित करते हैं, जिससे $1.65 \mu\text{mol h}^{-1}$ की हाइड्रोजन उत्पादन दर और 840 एनएम पर 5.43% की स्पष्ट क्वॉंटम उपज प्राप्त होती है। इसके अतिरिक्त, हम खोखली संरचनाओं की तुलना में जर्दी@शेल नैनोस्ट्रक्चर के महत्व को रेखांकित करते हैं, खोज से पता चलता है कि जर्दी@शेल नैनोस्ट्रक्चर खोखले की तुलना में काफी उच्च हाइड्रोजन उत्पादन दर दिखाते हैं, क्योंकि योक@शेल कॉन्फिगरेशन में एयू कोर और के बीच इलेक्ट्रॉन हस्तांतरण बढ़ता है। Ag/AgCuS शेल, इंटरफ़ेस पर ऊपर की ओर बैंड झुकने से सुगम होता है, जैसा कि पराबैंगनी फोटोइलेक्ट्रॉन स्पेक्ट्रोस्कोपी (UPS) द्वारा पुष्टि की गई है। यह अध्ययन जर्दी@शेल नैनोस्ट्रक्चर के महत्व और पीसी हाइड्रोजन उत्पादन पर शून्य स्थान के प्रभाव को रेखांकित करता है।

अध्याय 6 में, Cu/In अनुपात को ट्यून करके, हम Au@CuInS₂ (Au@CIS) जर्क@शेल नैनोस्ट्रक्चर में पीसी हाइड्रोजन उत्पादन दर निर्धारित करने में धनायन अनुपात की भूमिका को स्पष्ट करते हैं। मैट्रिक्स के भीतर तांबे के सापेक्ष बढ़ी हुई इंडियम सामग्री कार्य फंक्शन को बढ़ाती है, जिससे हाइड्रोजन उत्पादन दर में वृद्धि होती है। इस सुधार का श्रेय Au कोर और CuInS₂ योक के बीच कुशल चार्ज ट्रांसफर को दिया जाता है, जो इंटरफ़ेस पर ऊपर की ओर झुकने वाले बैंड द्वारा सुगम होता है। यह अध्ययन पीसी हाइड्रोजन उत्पादन पर धनायन अनुपात के महत्वपूर्ण प्रभाव पर प्रकाश डालता है।

कुल मिलाकर, यह थीसिस धातु-ऑक्साइड और धातु सल्फाइड अर्धचालकों के गुणों को उनके फोटोइलेक्ट्रोकेमिकल (पीईसी) और फोटोकैटलिटिक (पीसी) हाइड्रोजन दक्षता को बढ़ावा देने के लिए विभिन्न रणनीतियों का उपयोग करके ट्यून करने के लिए समर्पित है।

CONTENT

Content	iii
CERTIFICATE	iv
ACKNOWLEDGEMENTS	v
Abstract	vii
Content	x
LIST OF FIGURES	xiii
LIST OF TABLES	xix
COMPENDIUM OF SYMBOLS AND ABBREVIATIONS	xx
Chapter 1	1
Introduction	1
1.1 Background and Motivation	1
1.2 Renewable Energy Resources	2
1.3 Photoelectrochemical (PEC) and Photocatalytic (PC) Water Splitting	5
1.4 Criteria for selection of Semiconductor Material	7
1.5 Material selection	9
1.5.1 Investigation of g-C ₃ N ₄	9
1.5.2 Investigation of Fe ₂ O ₃	11
1.5.3 Metal Sulfides Yolk@Shell nanostructure for PC H ₂ Generation	13
1.6 Thesis Reorganization	16
1.7 References	18
Methodology and Characterization	30
2.1 Synthesis Method	30
2.1.1 Synthesis of g-C ₃ N ₄ , NiO and their nanocomposite (Ni/NiO/g-C ₃ N ₄)	30
2.1.2 Synthesis of Surface modified Fe ₂ O ₃ with MnO _x	31
2.1.3 Synthesis of Au@Ag/AgCus Yolk@shell nanostructures	32
2.1.4 Synthesis of Au@CuInS ₂ Yolk@shell nanostructures	33
2.2 Characterization Technique	35
2.2.1 X-ray Diffraction (XRD)	35
2.2.2 Raman Spectroscopy	36
2.2.3 Optical Properties	38
2.2.4 Scanning Electron Microscopy (SEM)	39

2.2.5	Energy Dispersive X-ray Spectroscopy (EDX)	40
2.2.6	Transmission Electron Microscopy (TEM).....	40
2.2.7	X-ray Photoelectron Spectroscopy.....	41
2.2.8	Ultra-violet Photoelectron Spectroscopy (UPS).....	42
2.3	Photoelectrochemical Measurements:	43
2.3.1	Linear Sweep Voltammetry:	45
2.3.2	Applied Bias to Photocurrent Efficiency	46
2.3.3	Electrochemical Impedance Spectroscopy	46
2.3.4	Mott-Schottky Measurement.....	48
2.4	Photocatalytic Hydrogen generation Experiment	50
2.5	References	52
Chapter 3.....		54
Uncovering the Role of Ni and NiO Towards Enhanced PEC Water Splitting Properties and Charge Dynamics of g-C₃N₄		54
Abstract		
3.1	Introduction:.....	55
3.2	Result & Discussion.....	56
3.3	Conclusion.....	74
3.4	References	75
Chapter 4.....		81
Mechanistic Insights into the Origin of MnO_x Co-Catalysts for the Improved Photoelectrochemical Properties of Fe₂O₃		81
Abstract		
4.1	Introduction	82
4.2	Results and discussion.....	84
4.3	Conclusions	99
4.4	References	100
Chapter 5.....		108
Investigation of the Impact of Void space in Au@Ag/AgCuS Yolk@Shell Nanostructures on Photocatalytic Hydrogen Evolution.....		108
Abstract		
5.1	Introduction	109
5.2	Results and discussion.....	110
5.3	Conclusion.....	122
5.4	References	123
Chapter 6.....		126

Exploring the Impact of Cu/In ratio of Au@CuInS₂ Yolk@Shell Nanostructure Towards Photocatalytic Hydrogen Evolution.....	126
Abstract	
6.1 Introduction	127
6.2 Result and discussion	128
6.3 Conclusion.....	138
6.4 References	139
Chapter 7.....	142
Conclusion and Future Perspective	142
7.1 Thesis Summary	142
7.2 Future Scope	144
7.3 References	146
Curriculum vitae	147

LIST OF FIGURES

Figure No.	Figure Caption	Page No.
1.1	<i>Analysis of global energy consumption trends from 2010 to 2050, detailing the contributions from various energy sources. Data adapted from the U.S. Energy Information Administration (EIA) website.</i>	1
1.2	<i>Average carbon dioxide (CO₂) levels from 1960 to 2023 at Mauna Loa, from the Scripps Institution for Oceanography, UC San Diego.</i>	2
1.3	<i>Schematic representation on of Photocatalytic (PC) and photoelectrochemical (PEC) water splitting using dispersed particles as a photocatalyst and n-type semiconductor as photoanode respectively.</i>	5
1.4	<i>Mechanism of the PC and PEC water splitting using semiconductor-based photocatalyst.</i>	8
1.5	<i>Different types of N and O functionalities present in g-C₃N₄.</i>	10
1.6	<i>Distribution of solar spectrum and band structure of metal oxides and sulfides.</i>	14
1.7	<i>Properties of yolk@shell nanostructures.</i>	16
2.1	<i>Schematic representation of thermally annealed g-C₃N₄, NiO and their nanocomposite (Ni/NiO/g-C₃N₄)</i>	31
2.2	<i>Schematic representation of the electrochemical synthesis of Fe₂O₃, and MnO_x/Fe₂O₃ t films.</i>	32
2.3	<i>Schematic representation of the synthesis of Fe₂O₃, and Au@Ag/AgCuS yolk@shell nanostructures.</i>	33

2.4	<i>Schematic representation of the synthesis of Fe₂O₃, and Au@CuInS₂ yolk@shell nanostructures.</i>	34
2.5	<i>Schematic representation of diffraction pattern in a crystal system</i>	35
2.6	<i>Schematic representation of Rayleigh and Raman scattering</i>	37
2.7	<i>Schematic representation of (a) a Photoelectrochemical (PEC) setup featuring a Teflon cell with a three-electrode configuration, and (b) a Photocatalytic (PC) setup comprising a quartz cell with an airtight sealed neck.</i>	44
3.1	<i>XRD pattern (a) for pristine g-C₃N₄, NiO, and nanocomposites and (b) FTIR spectra for pristine g-C₃N₄, NiO and nanocomposites.</i>	56
3.2	<i>FESEM images of (a) pristine g-C₃N₄ showing bulk layers structure, (b) pristine NiO showing spherical shape morphology, (c) (1:8) Ni/NiO/g-C₃N₄ showing a uniform distribution of NiO spherical particles over g-C₃N₄ sheet, and (d-e) element mapping of C, N, O, and Ni in (1:8) Ni/NiO/g-C₃N₄.</i>	58
3.3	<i>TEM images of (a) pristine g-C₃N₄, (b) pristine NiO, and (c) Ni/NiO/g-C₃N₄ nanocomposite.</i>	59
3.4	<i>Survey XPS spectra of pristine g-C₃N₄, pristine NiO, their all synthesize nanocomposite.</i>	59
3.5	<i>XPS spectra of (a) C 1s (pristine g-C₃N₄), (b) N 1s (pristine g-C₃N₄), (c) Ni 2p (pristine NiO) and (d) O 1s (pristine NiO), (e) C 1s (Ni/NiO/g-C₃N₄), and (f) Ni 2p Ni/NiO/g-C₃N₄).</i>	60
3.6	<i>XPS spectra of nanocomposites corresponding to C 1s {(a) (1:1) Ni/NiO/g-C₃N₄, (c) (1:4) Ni/NiO/g-C₃N₄, and (e) (1:12) Ni/NiO/g-C₃N₄, and Ni 2p {(b) (1:1) Ni/NiO/g-C₃N₄, (d) (1:4) Ni/NiO/g-C₃N₄ and (f) (1:12) Ni/NiO/g-C₃N₄.</i>	62
3.7	<i>XPS spectra of nanocomposites corresponding to N 1s {(a) (1:1) Ni/NiO/g-C₃N₄, (b) (1:4) Ni/NiO/g-C₃N₄, and (c) (1:8) Ni/NiO/g-C₃N₄}, and{(d) (1:12) Ni/NiO/g-C₃N₄}.}</i>	63

3.8	<i>(a) J-V polarization curves for pristine g-C₃N₄, pristine NiO, and nanocomposites recorded in 0.1 M KOH (pH = 12.3) electrolyte under darkness (dotted line) and light illuminations (solid line) at scan rate of 10 mV/s, (b) applied bias to photocurrent efficiency (ABPE), and (c) Nyquist plot for pristine g-C₃N₄, pristine NiO, and the nanocomposite recorded at 300 mV overpotential from 1-10⁶ Hz frequency range, and (d) UV-Visible absorption spectra of pristine g-C₃N₄, pristine NiO and their nanocomposites.</i>	65
3.9	<i>Mott-Schottky plot for g-C₃N₄, NiO, and the nano-composite recorded in dark at 1000Hz (b) Depletion layer width at 1.23 V vs RHE.</i>	66
3.10	<i>Light illumination on OCP for pristine NiO.</i>	67
3.11	<i>(a) LSVs recorded in 0.1 M KOH in dark (dotted line) and light (solid line) at scan rate of 10 mV/s and (b) Nyquist plot recorded at 300 mV overpotential in frequency range of 1-10⁶ Hz for 1:8 (Ni/NiO/g-C₃N₄) based electrodes synthesized as physical mixture, layer-by-layer deposition, and annealed composite.</i>	70
3.12	<i>(a) XPS survey spectrum and, (b) An overlap of core level spectra comparison of Ni 2p for (1:8) Ni/NiO/g-C₃N₄ for before and after PEC measurements.</i>	71
3.13	<i>Solid state PL spectra of pristine g-C₃N₄, pristine NiO and their nanocomposites.</i>	72
3.14	<i>(a) Time resolved PL of pristine g-C₃N₄, pristine NiO and their nanocomposites, (b) Schematic for band structure.</i>	73
4.1	<i>SEM images of (a) bare Fe₂O₃ and (b) Fe₂O₃/MnO_x 100 s. (c) and (d) showed the corresponding XRD patterns and Raman spectra.</i>	85
4.2	<i>(a) XRD patterns of pristine FTO and bare MnO_x. (b) Raman spectrum of bare MnO_x.</i>	86
4.3	<i>(a) XPS survey spectra for bare Fe₂O₃ and Fe₂O₃/MnO_x 100 s. XPS spectra of (b) O 1s, (c) Fe 2p, and (d) Mn 2p core levels for Fe₂O₃/MnO_x 100 s.</i>	87
4.4	<i>(a) J-V curves recorded on bare Fe₂O₃ and various Fe₂O₃/MnO_x under dark and light illumination. (b) Corresponding I-t curves</i>	89

recorded under chopped light illumination. (c) Comparative *I-t* curves for bare Fe_2O_3 , bare MnO_x and Fe_2O_3/MnO_x 100 s. (d) Nyquist plots recorded on bare Fe_2O_3 and various Fe_2O_3/MnO_x . (e) and (f) showed the equivalent circuits used for data fitting for bare Fe_2O_3 and various Fe_2O_3/MnO_x , respectively

- 4.5** SEM images of (a) bare Fe_2O_3 , (b) Fe_2O_3/MnO_x 100 s, and (c) Fe_2O_3/MnO_x 150 s. In (a), the surface cracks were highlighted with square marks, (d) CV curves of pristine FTO and bare Fe_2O_3 recorded in 0.1 M KCl and 10 mM $K_4[Fe(CN)_6]$ solution at 10 mV/s scan rate. 91
- 4.6** (a) XPS spectra of Mn 2p for bare MnO_x and Fe_2O_3/MnO_x 150 s. (b) J-V curves recorded on bare MnO_x and Fe_2O_3/MnO_x 150 s under darkness. 92
- 4.7** (a) CV curves recorded on (a) bare Fe_2O_3 and (b) Fe_2O_3/MnO_x 100 s with a varying scan rate from 10 to 100 mV/s. (c) Corresponding capacitive current density (ΔJ) for bare Fe_2O_3 and Fe_2O_3/MnO_x 100 s as a function of scan rate. (d) Mott-Schottky plots for bare Fe_2O_3 and Fe_2O_3/MnO_x 100 s. 93
- 4.8** J-V curves recorded on (a) bare Fe_2O_3 and (b) Fe_2O_3/MnO_x 100 s in KOH electrolyte containing Na_2SO_3 under light illumination. (c) Comparison of hole injection efficiency for bare Fe_2O_3 and Fe_2O_3/MnO_x 100 s. 95
- 4.9** (a) UV-visible diffuse reflectance spectra and (b) calculated band gap from Tauc plots for bare Fe_2O_3 and Fe_2O_3/MnO_x 100 s. 96
- 4.10** (a) J-V curves and (b) the corresponding *I-t* curves recorded on Fe_2O_3/MnO_x 100 s under chopped light illumination after it was annealed at 350 °C and 550 °C. 96
- 4.11** *I-t* curves recorded on Fe_2O_3/MnO_x 100 s under chopped light illumination. 97
- 4.12** Mechanistic illustration of the function of the deposited MnO_x for the improved PEC performance of Fe_2O_3 . 98
- 5.1** Schematic illustration of synthetic procedures for Au@AgCuS 111

5.2	<i>(a) TEM images of (a) Au@Ag/AgCuS-2, (b) Au@Ag/AgCuS-3, (c) pure Ag/AgCuS. (d) XRD patterns of Au@Cu₇S₄ and Au@Ag/AgCuS-3.</i>	112
5.3	<i>(a) TEM image, (b) low-magnitude TEM image and the corresponding TEM-EDS mapping profile for Au@Ag/AgCuS-3.</i>	113
5.4	<i>Absorption spectra for (a) Au@Ag/AgCuS-2, Au@Ag/AgCuS-3, and pure Ag/AgCuS nanostructure, and (b) pure Au NP colloidal.</i>	114
5.5	<i>TA spectra and kinetics traces of (a, d) Ag/AgCuS, (b, e) Au@Ag/AgCuS-2, (c, f) Au@Ag/AgCuS-3.</i>	116
5.6	<i>UPS spectra for (a), (b) pure Ag/AgCuS and pure Au.</i>	117
5.7	<i>XPS spectra of (a) Cu 2p, and (b) for S 2p for Au@Ag/AgCuS-3, and Au@Cu₇S₄.</i>	118
5.8	<i>(a) Constructed band structure and (b) band alignment for Au@Ag/AgCuS.</i>	119
5.9	<i>(a) Hydrogen production results for relevant samples under visible light irradiation. (b) Wavelength-dependent AQY spectra for Au@Ag/AgCuS-3 and pure Ag/AgCuS.</i>	120
5.10	<i>(a) Stability cycles for hydrogen generation for Au@Ag/AgCuS, (b-c) FE-SEM images for fresh and used Au@Ag/AgCuS-3 nanostructure, (d) Cu 2p core level XPS spectra, (d) Ag 3d core level XPS spectra, and (f) S 2p core level XPS spectra of Au@Ag/AgCuS. photocatalyst before and after hydrogen generation.</i>	121
6.1	<i>Schematic illustration of synthetic procedures for Au@CuInS₂</i>	128
6.2	<i>(a) TEM images of (a) Au@CIS-1, (b) Au@CIS-2, (c) Au@CIS-3, and (d) XRD patterns of all Au@CIS.</i>	129
6.3	<i>(a) Absorption spectra for (a) Au@CIS-1, Au@CIS-2, Au@CIS-3, and pure CIS yolk@shell nanostructure, (b) absorption spectra for pure Au NP colloidal, and (c, d, e) corresponding Taue plot for Au@CIS-1, Au@CIS-2, Au@CIS-3 respectively.</i>	131

6.4	<i>UPS spectra for (a, b) CIS-1, (c, d) CIS-2, (e, f) CIS-3, and (g) Pure Au Np respectively.</i>	132
6.5	<i>Band structure illustration based on UPS data for CIS-1, CIS-2, and CIS-3, respectively.</i>	133
6.6	<i>(a) Cu 2p, and (b) In 3d xps spectra for Au@Cu₇S₄ and all Au@CIS samples.</i>	134
6.7	<i>Band alignment for Au@CIS-2, Au@CIS-3 and (c) hydrogen generation rate for Au@Cis-2, and Au@CIS-3 respectively.</i>	135
6.8	<i>Hydrogen production results for relevant samples under visible light irradiation. (b) Wavelength-dependent AQY spectra for Au@CIS-3 and pure CIS from 300-800 nm.</i>	137
6.9	<i>(a) stability cycles for hydrogen generation for Au@CIS-3, (b) XRD pattern for fresh and used sample Au@CIS-3(c, d) Cu 2p and In 3d core level XPS spectra for fresh and used sample Au@CIS-3, (e, f) FE-SEM images for fresh and used Au@Au@CIS-3.</i>	138

LIST OF TABLES

Table No.	Table Caption	Page No.
3.1	<i>Summary of fit parameters and goodness of fit information for time-resolved photoluminescence plots shown in Figure 3.13 for pristine g-C₃N₄, pristine NiO, and nanocomposites.</i>	73
5.1	<i>EDX analysis for Au@Ag/AgCuS-2, Au@Ag/AgCuS-3, and pure Ag/AgCuS nanostructure.</i>	113
6.1	<i>Induced coupled plasmon mass spectroscopy analysis for all Au@CIS samples</i>	130
6.2	<i>Description of particle size, shell thickness and void space for all Au@CIS samples.</i>	130

COMPENDIUM OF SYMBOLS AND ABBREVIATIONS

PEC	Photoelectrochemical water splitting
PC	Photocatalysis
HER	Hydrogen Evolution Reaction
OER	Oxygen Evolution Reaction
VBM	Valence Band Maxima
CBM	Conduction Band Minima
EF	Fermi Level
LSV	Linear Sweep Voltammetry
CV	Cyclic Voltammetry
EIS	Electron Impedance Spectra
MS	Mott-Schottky
AQY	Apparent Quantum Yield
g-C ₃ N ₄	Graphitic Carbon Nitride
NiO	Nickel Oxide
Fe ₂ O ₃	Hematite

MnO _x	Manganese Oxide
L-AA	L-Ascorbic Acid
NaOH	Sodium Hydroxide
Na ₂ S	Sodium Sulfide
TOP	Trioctylphosphine
InCl ₃	Indium chloride
Hcl	Hydrochloric Acid
Cu	Copper
In	Indium
Au	Gold Nanoparticles
Au@Ag/AgCu	Gold@Silver/Silver Copper Sulfide
Au@CIS	Gold@Copper Indium Sulfide
SPR	Surface Plasmon Resonance
LSPR	Localized Surface Plasmon Resonance
h	Hour
min	Minute

s	Second
ns	Nanosecond
ps	Picosecond
g	Gram
eV	Electron volt
°C	Degree Centigrade
M	Molar
mmol	Millimole
μmol	Micromole
E_g	Band Gap
mL	Milliliter
λ	Wavelength
Ar	Argon
H ₂	Hydrogen Gas
K _{sp}	Solubility Product
CO ₂	Carbon Dioxide

XRD	X-Ray diffraction
U.V.	U.V Visible Spectroscopy
TEM	Transmission Electron Microscopy
SEM	Scanning Electron Microscopy
EDX	Energy Dispersive X-ray Spectroscopy
XPS	X-ray Photoelectron Spectroscopy
UPS	UV Photoelectron Spectroscopy
TA	Transient Absorption Spectroscopy
GC	Gas Chromatography
ICP-MS	Induced Couple Plasma-Mass Spectroscopy